Adhesion Failure at 180 000 Frames per Second: Direct Observation of the Detachment Process of a Mushroom-Shaped Adhesive

Lars Heepe,[1] Alexander E. Kovalev,[1] Alexander E. Filippov,[1,2] and Stanislav N. Gorb[1]

[1]*Functional Morphology and Biomechanics, Zoological Institute, Kiel University, Am Botanischen Garten 1-9, 24118 Kiel, Germany*
[2]*Donetsk Institute for Physics and Engineering of the National Academy of Sciences of the Ukraine, Donetsk 34083, Ukraine*

Nature has successfully evolved the mushroom-shaped contact geometry in many organisms in order to solve the attachment problem. We studied the detachment process of individual bioinspired artificial mushroom-shaped adhesive microstructures (MSAMSs) resolving the failure dynamics at high spatio-temporal resolution. The experimental data provide strong evidence for a homogeneous stress distribution in MSAMS, which was recently proposed. Our results allow us to explain the advantage of such contact geometry and provide a suggestion for the widely observed mushroom-shaped contact geometry.

Adhesion between two surfaces is a phenomenon of fundamental importance to our everyday life not only in practical applications such as sticky tapes or joining the components in various technological processes. It also has strong relevance to biological systems (e.g., cell adhesion [1], superhydrophobicity [2], gecko adhesion [3,4]), in technical systems involving friction [5] (e.g., road-tire contact), or in the fabrication of surface micro- and nanomechanical structures [6]. Whether the surfaces adhere chemically (chemical bonds) or physically (e.g., van der Waals interaction), failure, i.e., the breaking of bonds, usually occurs by front propagation in the interface and has received much attention [7–9]. Surface roughness is known to mainly control adhesion between two contacting bodies because it generally prevents the formation of intimate contact [7]. In addition, the contact geometry of two contacting bodies was shown to greatly control adhesion [10,11].

Interestingly, in living nature the mushroom-shaped contact geometry for attachment has been independently developed at the macro, micro, and nano scale in the evolution of many organisms from different lineages (animals, plants, fungi, and bacteria) living in both terrestrial and aquatic environments [12]. This very specific geometry suggests an evolutionary adaptation and optimization to the attachment problem. The mushroom-shaped contact geometry is similar to the flat punch geometry [Fig. 1(a)], consisting of a stalk but having a widened contact plate [Fig. 1(b)]. At the nanometer scale, for example, the bacterium *Caulobacter crescentus* attaches to surfaces via so-called adhesive holdfasts resembling the mushroom-shaped contact geometry and it was shown to produce one of the highest ever measured adhesion strength of biological adhesives [13]. At the micro scale, animals, such as some insects and spiders, have evolved mushroom-shaped contact geometry to adhere to and run on walls and ceilings [4]. They were shown to perform especially well on smooth surfaces [14] and bio-inspired adhesive tapes with such contact geometry even

outperform the spatula-shaped geometry of geckos under certain conditions [11].

However, a fundamental understanding of the advantages of the mushroom-shaped contact geometry is still vague. So far experiments of the detachment behavior of mushroom-shaped adhesive elements revealed a different failure mode if compared to the flat punch geometry where crack propagation starts at the outer edge, further called mode I (not to be confused with the fracture mode from fracture mechanics), due to stress concentration [inset Fig. 1(a)] [12]. In mushroom-shaped adhesive elements detachment was observed to occur first by crack nucleation somewhere in the middle of the contact interface, further called mode II, and subsequent crack propagation towards the outer edge while the perimeter remained in contact until complete separation [see Fig. 1(b)] [15–17]. This type of failure is in agreement with calculations of the normal stress distribution at the contact interface between a mushroom-shaped adhesive element and a flat substrate using finite element analysis. The stress was shown to be homogeneous under the stalk without the typical edge stress concentrations [inset Fig. 1(b)] as in the flat punch geometry [13]. Only recently, Carbone and co-workers proposed a first theoretical model capturing the physical mechanisms of enhanced adhesion of this mushroom-shaped contact geometry compared to the flat punch geometry [18]. They also showed that depending on the actual geometrical parameters the thin contact lip of mushroom-shaped elements reduces or even eliminates the edge stress concentration of the stalk and showed that the experimentally found mode II failure is the favored mechanism in detachment of mushroom-shaped microstructures for a broad range of geometrical parameters [19]. The main result was the mode II pull-off stress given by [18]

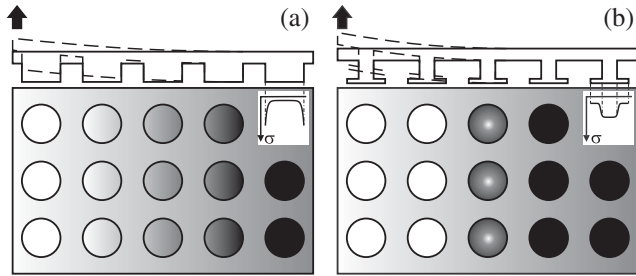$$\sigma = \left(\frac{\pi \Delta \gamma E^*}{2a}\right)^{1/2},$$ (1)

FIG. 1. Detachment of two differently microstructured adhesive tapes. Although similar crack propagation at the global scale is observed, illustrated by the background shading from bright (detachment) to dark (attached), crack propagation is completely different at the local scale (see shading of individual structures). (a) In the flat punch contact geometry adhesive failure starts at the perimeter due to edge stress concentrations (see inset). (b) In the mushroom-shaped contact geometry the thin contact plate eliminates the edge stress concentration leading to a homogeneous stress distribution (see inset) changing the adhesive failure mode.

where $\Delta\gamma$ is an effective work of adhesion (for rubberlike materials usually much larger than the Dupré energy of adhesion $\Delta\gamma_0$ [20]), $E^* = E/(1 - \mu^2)$ is the reduced elastic modulus, μ is Poisson's ratio, and $2a$ is the size of a preexisting crack. Although promising agreement with recently reported adhesion data, this model assumes preexisting defects of 3–4 μm in the contact interface [18]. This assumption, however, must not necessarily be fulfilled in real experiments where no observable defect exists.

In this Letter, we present the first detailed study on the detachment behavior of individual mushroom-shaped adhesive microstructures (MSAMSs) [21,22] resolving the complete failure dynamics with high spatiotemporal accuracy. We find detachment to be a three-phasic process where first the contact area of individual MSAMSs shrinks up to 25%, followed by interfacial crack nucleation and quasistatic crack propagation. At a critical crack size the system destabilizes and spontaneous failure with crack propagation velocities as high as 15% of the Rayleigh wave velocity of the material are found. Finally, we show that our experimental results can be well described by the Carbone model even without preexisting defects but considering the size of those as the critical dynamic crack size where the system becomes unstable.

We describe here experiments where three individual MSAMSs, denoted by 1–3, were detached from a smooth glass slide simultaneously recording the spatiotemporal failure dynamics. Individual MSAMSs were cut off from the tape made from polyvinylsiloxane (PVS) with a thickness of the supporting polymer film of about 900 μm [21]. Detachment behavior was recorded using a high-speed camera Photron Fastcam SA1.1 installed on an upright light microscope operated in epi-illumination mode. Figure 2(a) shows the schematic of the experimental setup. To be able to repeatedly attach and detach individual MSAMSs, they
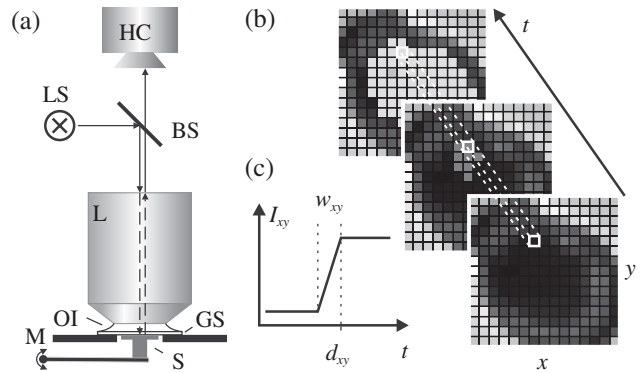

FIG. 2. (a) Schematic of the experimental setup. HC, high-speed camera; LS, light source; BS, beam splitter; L, lens; OI, oil immersion; GS, glass slide; S, sample; M, manipulator. (b) Schematic of the video analysis procedure. Within a whole sequence, pixelwise, the change in intensity I_{xy} is observed. (c) Representative intensity profile for a pixel in which MSAMS was first in direct contact with the glass (low intensity). The gradual increase (transition) in intensity corresponds to the propagation of the crack over the pixel area with a duration of w_{xy} until the contact is lost (high intensity) at d_{xy}.

were glued to a three-axis manipulator Kleindiek MM3A LS. To ensure parallel alignment between the samples and the glass slide, individual MSAMSs were first attached to the glass slide manually by a pair of tweezers observing the proper contact via the microscope. Then, attached to the glass slide, samples were withdrawn at a retraction velocity $v_r = 50\ \mu$m/s $\pm\ 7\ \mu$m/s. Detachment was first recorded at 5400 frames/s and sequences were analyzed manually using ImageJ measuring the contact area A at ten positions from the first frame prior withdrawal A_0 to the last frame prior complete detachment A_{det}.

Surprisingly, the very moment of detachment could not be resolved properly for all samples 1–3. Figure 3 shows
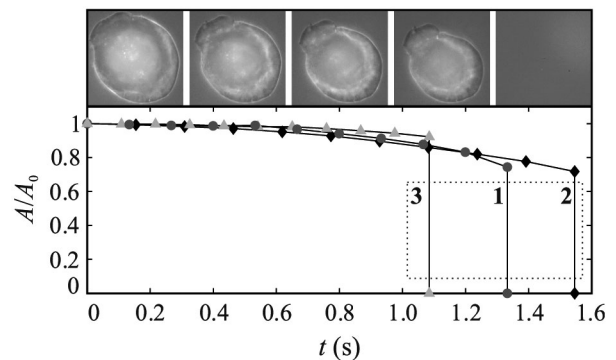

FIG. 3. Normalized contact area of MSAMSs 1–3 as a function of time t. Data were obtained from individual frames of high-speed video recordings at 5400 frames/s. The very moment of detachment could not be properly resolved as indicated by the sharp transition (dashed box). The decrease in contact area was almost entirely due to shrinkage without losing contact (see still images).

the normalized contact area A/A_0 first decreasing up to 25% followed by a sharp transition (see dashed box). Reduction in contact area was almost entirely due to shrinkage without losing contact (see still images Fig. 3). A judgment of the actual failure mode was almost impossible.

In order to resolve the very moment of detachment individual MSAMSs were reattached and detachment was now recorded at 180 000 frames/s. These high-speed sequences were analyzed to quantify the spatiotemporal failure dynamics of the detachment of individual MSAMSs using the following procedure (a similar approach was suggested in Refs. [8,9]): Due to considerable noise in the high-speed video recordings the extraction of crack fronts could not reliably be performed by imposing a simple threshold upon each frame. Therefore, we here locally recognized the temporal course of the intensity I_{xy} (gray-scale value) for each pixel within a sequence [see Fig. 2(b)]. Figure 2(c) shows a typical, idealized intensity profile of a pixel in which MSAMS was in direct contact with the glass (low intensity). The gradual increase (transition) in intensity corresponds to the propagation of the crack over the pixel area until the contact was lost (high intensity). By fitting these curves with a sigmoid function the points in time detachment occurred in each pixel d_{xy} were obtained forming the spatiotemporal detachment matrix $\mathbf{D}(x, y)$.

In addition, local crack propagation velocities v_{xy} were calculated forming the spatiotemporal velocity matrix $\mathbf{V}(x, y)$. In principle this could have been easily calculated by $(1/w_{xy})(l/\delta t)$, where w_{xy} is the width of the transition (time the crack propagates over the pixel area), l is the pixel length (here $\sim$330 nm), and δt is the temporal resolution (inverse of the frame rate). However, despite the high temporal resolution of $\delta t = 5.5$ μs local crack propagation velocities were usually much larger than $l/\delta t$ (upper resolution limit per pixel); i.e., crack propagated more than one pixel from frame to frame. Thus, we here estimated local crack propagation velocities at the crack fronts obtained from $\mathbf{D}(x, y)$ by setting the matrix elements d_{xy} equal to one for $d_{xy} > t$ and zero elsewhere, where t runs (in units of δt) from $\min[\mathbf{D}(x, y)] < t < \max[\mathbf{D}(x, y)]$. Results were binary matrices from which crack fronts could be easily extracted. Assuming the crack takes the shortest path from one front to the next front, local crack propagation velocities could be calculated by the time interval between these two fronts.

Figure 4 shows the results obtained from the high-speed video recordings. Figures 4(a)–4(c) show MSAMSs 1–3 in contact with the glass slide (dark region). The contact area below the stalk [indicated by the dashed line in Fig. 4(a)] appears even darker. Sample 1 [Figs. 4(a)] had a preexisting crack (PC) outside this area. Sample 3 [Fig. 4(c)] had a PC within this area. Color-coded spatiotemporal detachment maps $\mathbf{D}(x, y)$ [Figs. 4(d)–4(f)] indicated mode II
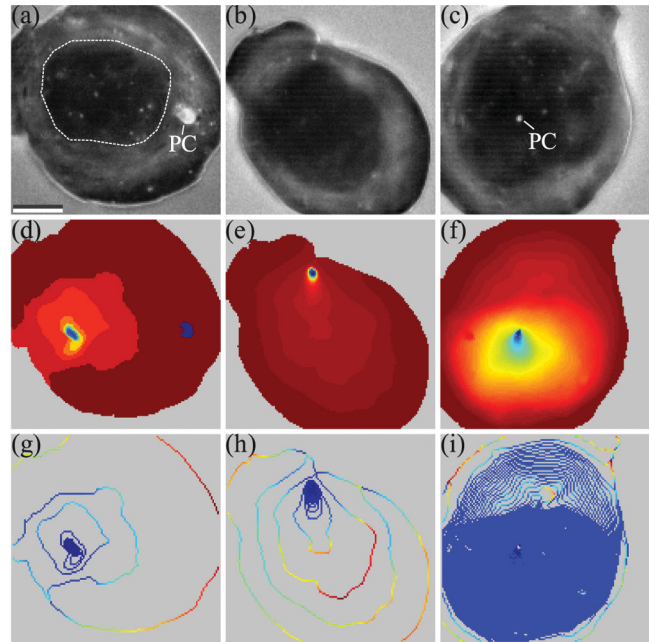

FIG. 4 (color). (a),(b),(c) MSAMS 1, 2, 3 in contact with the glass (dark area), respectively. Contact below the stalk appears darker indicated by the dashed line in (a). Sample 1 (a) had a PC outside the contact area below the stalk. Sample 3 (c) as well had a PC, but within the contact area below the stalk. (d),(e), (f) Color-coded $\mathbf{D}(x, y)$ of samples 1, 2, 3, respectively. Blue regions detached first, red regions detached last, and areas sharing the same color detached at the same time. (g),(h), (i) Color-coded $\mathbf{V}(x, y)$ of samples 1, 2, 3, respectively. Scale bar of 10 μm applies to all images.

failure for all samples. Blue regions detached first (or PC), red regions detached last, and regions sharing the same color detached at the same time. This is in agreement with recent theoretical predictions for the mushroom-shaped contact geometry to detach in mode II especially in the case of an optimal geometry, i.e., when the ratio of the widened contact plate radius R_c and the stalk radius R_s is between $2 \leq R_c/R_s \leq 3$ [19]. In order to eliminate the edge stress concentration at the stalk radius the ratio $t(R_s)/R_s \geq 0.3$ with $t(R_s)$ the contact plate thickness at R_s [19]. Further, to avoid stress concentration at the contact plate edge $t(R_c)/R_s \leq 0.2$ [19]. For our samples $R_c/R_s \approx 2$, $t(R_s)/R_s \approx 0.50$, and $t(R_c)/R_s \approx 0.16$, thus MSAMSs used in this study are close to the optimal shape. The fact that crack nucleation did not start at the PC in sample 1 confirms that the thin contact plate does not support significant load as theoretically predicted [18]. It is interesting to note that the detachment pattern [Figs. 4(d)–4(f)] of repeated pull-off looks essentially the same for individual samples (compare videos S2 to S2_2nd and S3 to S3_2nd in the Supplemental Material [23]). Thus, detachment is predefined by the interfacial properties and thus mainly by the surface topography. So, it should be in principle possible to predict detachment by knowing the exact topography (which could be measured by, e.g., atomic

force microscopy). Duration of the actual detachment, i.e., from crack nucleation to complete separation, varied by 67, 656, and 2672 μs for samples 1, 2, and 3, respectively, which is 1–3 orders of magnitude faster than reported in Refs. [15,16,24]. Figures 4(g)–4(i) show the color-coded spatiotemporal velocity map $\mathbf{V}(x, y)$. The highest propagation velocity was observed in sample 1 with 2.68 m/s (1.75 m/s and 0.63 m/s for samples 2 and 3, respectively). This is about 15% of the Rayleigh wave velocity c_R of PVS [25]. We also performed the experiments with different retraction velocities, but already at $v_r = 1$ mm/s the very moment of detachment could not be resolved even with 450 000 frames/s, which corresponds to an average propagation velocity of approximately $0.6c_R$.

Figure 5 summarizes the data of the temporal course of the contact area A and the average crack velocity $\langle v \rangle$ (averaged over one crack front) obtained from Fig. 4. With 180 000 frames/s it was possible to resolve the very moment of detachment, i.e., the sharp transition shown in Fig. 3 (dashed box). Within the actual detachment process, i.e., from crack nucleation to complete detachment, we observed two distinct regimes separated by a sharp transition: first, quasistatic crack growth is observed, then the system destabilized followed by a regime with rapidly increasing crack velocities. It is interesting to note that at similar retraction velocities, in the flat punch geometry, crack velocities at the point of highest pull-off force were only in the range of μm/s [28]. Here, even prior to the point of instability (likely the point at highest pull-off force) crack velocities were in the range of cm/s and thus 2 orders of magnitude higher. This again reflects
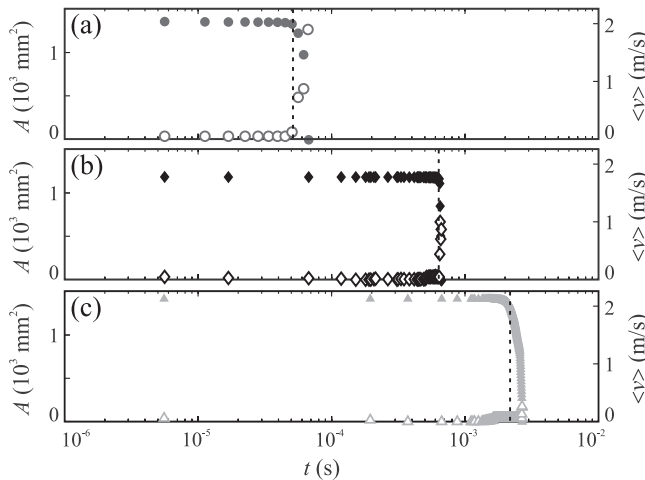
the homogeneous (optimized) stress distribution of MSAMS compared to the flat punch geometry because the higher amount of elastically stored energy in the contact interface allows for faster crack propagation.

We calculate pull-off forces $F_{\text{pull-off}}$ of samples 1–3 by $F_{\text{pull-off}} = k_{\text{eff}} v_r t$ where t is the duration of the whole detachment process obtained from Fig. 3. With Young's modulus $E = 1.5$ MPa [26], Poisson's ratio $\mu \simeq 0.49$, and using the geometrical parameter of individual MSAMSs described in Ref. [21] we estimate the effective stiffness of the samples to $k_{\text{eff}} \simeq 5$ N/m. We obtain 333, 387, and 271 μN for samples 1, 2, and 3, respectively. Using $\sigma = F_{\text{pull-off}}/A_{\text{det}}$ (A_{det} obtained from Fig. 3), $\Delta\gamma = 60$ mJ/m^2 (a typical experimentally obtained value [21,26]), and rearranging Eq. (1) with respect to the crack size we obtain the critical crack size a_c where the system becomes unstable by

$$a_c = \frac{\pi}{2} \frac{\Delta\gamma E^*}{F_{\text{pull-off}}^2} A_{\text{det}}^2. \tag{2}$$

We obtain 3.0, 2.0, and 7.0 μm for samples 1, 2, and 3, respectively. We observe good agreement if comparing the experimentally obtained points of instability and the theoretically predicted ones assuming a circular defect; see Fig. 5. Dashed lines in Fig. 5 correspond to the critical crack size calculated by Eq. (2). It is important to mention that the model presented in Ref. [18] predicts for a given preexisting crack size a a certain pull-off stress that diverges for smaller a; see Eq. (1). Evidently, from sample 2 and Ref. [15] there must not be (observable) PCs. Even though there is a PC, Eq. (1) seems to overestimate the pull-off force. For example, for sample 3 with a PC of $a \approx l$ in the contact area under the stalk we measured a pull-off force of 271 μN. Using Eq. (1), we obtain a pull-off force of about 1.25 mN, which is larger by more than a factor of 4 than the measured one. However, Eqs. (1) and (2) describe well the experimental results when interpreting the critical crack size a_c as a critical dynamic quantity. It seems to be also valid in case of no (observable) PC and must not coincide with the size of any PC.

In general, for rubberlike materials $\Delta\gamma$ may strongly increase by several orders of magnitude with increasing crack velocity due to viscoelastic energy dissipation and/or increased temperature in front of the crack tip. This effect is already relevant at velocities in the range of cm/s. In addition, inertia effects might be relevant already for the observed high crack velocities in the m/s range [20,29]. Evidently, the typical, experimentally obtained value for $\Delta\gamma$ is about 2–3 times higher than the Dupré energy of adhesion $\Delta\gamma_0$, calculated from the surface energies of PVS and glass [30]. However, the velocity dependence $\Delta\gamma(v)$ seems to be less pronounced than, e.g., for pressure sensitive adhesives [20].

To summarize, we have studied the detachment behavior of individual mushroom-shaped adhesive elements at high

FIG. 5. (a),(b),(c) Contact area A (filled symbols) and average crack velocity $\langle v \rangle$ (open symbols), shown from the moment of crack nucleation to complete separation, obtained from the data shown in Fig. 4 for samples 1, 2, 3, respectively. Actual detachment durations were 67, 656, and 2672 μs for samples 1, 2, 3, respectively. Dashed lines correspond to the critical dynamic crack size a_c predicted by Eq. (2).

spatiotemporal resolution. We have showed the dynamics of detachment from crack nucleation to complete separation. The experimental data provide strong evidence for the homogeneous (optimized) stress distribution of MSAMS and can be well described by a recent theoretical model. Thus, our experiment provides an explanation for the widely observed mushroom-shaped contact geometry in nature for the attachment problem.

[1] Y.-S. Chu, S. Dufour, J. P. Thiery, E. Perez, and F. Pincet, Phys. Rev. Lett. **94**, 028102 (2005).

[2] W. Barthlott and C. Neinhuis, Planta **202**, 1 (1997).

[3] K. Autumn, Y. Liang, S. Hsieh, W. Zesch, W. Chan, T. Kenny, R. Fearing, and R. Full, Nature (London) **405**, 681 (2000).

[4] S. N. Gorb, *Attachment Devices of Insect Cuticle* (Springer, New York, 2001).

[5] B. N. J. Persson, Phys. Rev. Lett. **89**, 245502 (2002).

[6] R. Maboudian and R. Howe, J. Vac. Sci. Technol. B **15**, 1 (1997).

[7] A. G. Peressadko, N. Hosoda, and B. N. J. Persson, Phys. Rev. Lett. **95**, 124301 (2005).

[8] K. J. Måløy, S. Santucci, J. Schmittbuhl, and R. Toussaint, Phys. Rev. Lett. **96**, 045501 (2006).

[9] K. T. Tallakstad, R. Toussaint, S. Santucci, J. Schmittbuhl, and K. J. Måløy, Phys. Rev. E **83**, 046108 (2011).

[10] R. Spolenak, S. Gorb, H. Gao, and E. Arzt, Proc. R. Soc. A **461**, 305 (2005).

[11] A. del Campo, C. Greiner, and E. Arzt, Langmuir **23**, 10235 (2007).

[12] S. N. Gorb and M. Varenberg, J. Adhes. Sci. Technol. **21**, 1175 (2007).

[13] P. H. Tsang, G. Li, Y. V. Brun, L. B. Freund, and J. X. Tang, Proc. Natl. Acad. Sci. U.S.A. **103**, 5764 (2006).

[14] D. Voigt, J. M. Schuppert, S. Dattinger, and S. N. Gorb, J. Insect Physiol. **54**, 765 (2008).

[15] M. Varenberg and S. Gorb, J. R. Soc. Interface **5**, 785 (2008).

[16] M. P. Murphy, B. Aksak, and M. Sitti, Small **5**, 170 (2009).

[17] In Refs. [15,16], the authors used arrays of mushroom-shaped adhesive elements that might not allow quantification of failure dynamics of individual elements due to collective effects.

[18] G. Carbone, E. Pierro, and S. N. Gorb, Soft Matter **7**, 5545 (2011).

[19] G. Carbone and E. Pierro, Small **8**, 1449 (2012).

[20] B. N. J. Persson, O. Albohr, G. Heinrich, and H. Ueba, J. Phys. Condens. Matter **17**, R1071 (2005).

[21] S. Gorb, M. Varenberg, A. Peressadko, and J. Tuma, J. R. Soc. Interface **4**, 271 (2007).

[22] L. Heepe, A. Kovalev, M. Varenberg, J. Tuma, and S. Gorb, Theor. Appl. Mech. Lett. **2**, 014008 (2012).

[23] See Supplemental Material at http://link.aps.org/supplemental/10.1103/PhysRevLett.111.104301 for details.

[24] L. Heepe, M. Varenberg, Y. Itovich, and S. N. Gorb, J. R. Soc. Interface **8**, 585 (2011).

[25] Using Young's modulus $E = 1.5$ MPa [26], Poisson's ratio $\mu \simeq 0.49$, and the density $\rho \simeq 1300$ kg/m^3, we find $c_R \simeq 0.91 c_s = 17.9$ m/s, where c_s is the shear sound velocity [27].

[26] F. Borodich, B. Galanov, S. Gorb, M. Prostov, Y. Prostov, and M. Suarez-Alvarez, Nanoscale Sys. **1**, 80 (2012).

[27] P. Vinh and R. Ogden, Wave Motion **39**, 191 (2004).

[28] U. Abusomwan and M. Sitti, Appl. Phys. Lett. **101**, 211907 (2012).

[29] G. Carbone and B. N. J. Persson, Phys. Rev. Lett. **95**, 114301 (2005).

[30] A. Peressadko and S. Gorb, J. Adhes. **80**, 247 (2004).